

Static and dynamic characterization of 3D-printed polymer structural elements

Mohammad Reza Khosravani ^{a,*}, Payam Soltani ^b, Bernard Rolfe ^c, Tamara Reinicke ^a, Ali Zolfagharian ^c

^a Chair of Product Development, University of Siegen, Paul-Bonatz-Str. 9-11, 57068 Siegen, Germany

^b System Engineering Department, Military Technological College (MTC), Muscat P.O Box 3214, Oman

^c School of Engineering, Deakin University, Geelong, Victoria 3216, Australia

ARTICLE INFO

Keywords:

Additive manufacturing
Bending tests
Free vibrations
FEM

ABSTRACT

Considering wide applications of Additive Manufacturing (AM), profound knowledge on the mechanical performance of AMed components is a necessity. In the present study, the mechanical behavior of AMed polymer parts under static and dynamic tests has been investigated. To this end, cantilever beams with three different mesostructure cells were designed and fabricated via ABS Carbon material based on the fused deposition modeling process. The specimens were subjected to a series of static bending tests and free vibration experiments. In addition, numerical models have been presented for both static bending and the dynamic tests. In the current study, digital image correlation technique has been employed to determine strain field and validate the numerical results. The experimental findings and numerical outcomes have been compared and the convergence has been investigated. Based on the applications of AM in fabrication of structural elements with complex geometries, the results of the current study are useful for new designs of AMed parts with customized mechanical strength and enhanced structural performance.

1. Introduction

Due to benefits of Additive Manufacturing (AM), this innovative manufacturing process has attracted considerable attention in recent years. AM, also known as three-dimensional (3D) printing, is a class of manufacturing technology that can be utilized for fabrication of physical objects directly from digital data. 3D printing is a tool-free technique that is suitable for fabrication of parts with complex geometries based on the principle of layered manufacturing. Moreover, this technique is flexible in design and it overcomes the design limitations related to subtractive manufacturing processes. Considering advantages and benefits of 3D printing, it has been used for fabrication of parts in different applications, such as medicine [1], electronics [2], food industry [3], construction [4], automotive [5], soft robotics [6], and aerospace industry [7]. According to ISO/ASTM 52900 [8], 3D printing has been classified into seven methods of which material extrusion is utilized in the present study.

Material extrusion is one of the most common 3D printing techniques for fabrication of customized engineering plastic parts. Fused Deposition Modeling (FDM) is a common material extrusion-based 3D printing process that uses different thermoplastics, such as Polylactic Acid (PLA), nylon, and Acrylonitrile Butadiene Styrene (ABS). In detail,

the FDM technique utilizes a continuous filament of a thermoplastic material that is fed from a coil, by moving of the hot extruder head. The pattern of each layer can be controlled by changing the position of the nozzle via mechanical manipulation. As FDM is affordable and easy-to-use, it has been used in diverse applications, and relatively growing number of scientific research works have been performed over the last ten years [9–12]. Considering applications of 3D-printed parts, the mechanical performance and structural integrity of 3D-printed components have become of great importance [13–15]. Although FDM-printed components have been used in different applications (as prototypes or final products), these parts have showed poor mechanical strength. Based on aforementioned issues, different research studies have been conducted to investigate mechanical behavior and fracture behavior of FDM-printed components [16–19]. For instance, in [20], we investigated effects of raster orientation and printing speed on the mechanical strength of FDM-printed parts. To this aim, the specimens with five different raster orientations were fabricated under two different printing speeds. Based on the tests, dependency of the mechanical strength and elastic modulus of the parts on the raster orientation has been documented. Moreover, the obtained results confirmed that the higher

* Corresponding author.

E-mail address: mohammadreza.khosravani@uni-siegen.de (M.R. Khosravani).

fracture load was belong to the samples fabricated at the lower speed. Later, thermal annealing and isostatic pressing process have been utilized to improve mechanical and surface properties of FDM-printed components [21]. In this context, thermal annealing was coupled with isostatic pressing. This post-processing has led to improvement in layer adhesion that was proved by enhancement in flexural modulus and flexural strength of the examined components.

In the FDM process, the printed parts are created by putting down filament that fused together chemically or thermally with the layer underneath. As a result, there is anisotropic material properties with void and weld in layers. A review of the literature reveals that different computer modeling of parts fabricated by the FDM process have been performed by various multi-scale methods [22–25]. For instance, in [26] the asymptotic theory of homogenization has been used to determine effective elastic moduli and strength of ABS 3D-printed parts. More recent studies [27–30], investigated failure mechanism of FDM 3D-printed components. An extant study [31] presents details of failure behavior in the FDM parts printed with different layer thicknesses. To this aim, experimental tests are carried out using ABS material, and different models are created to determine influence of the layer thickness on the mechanical behavior of the components.

The aim of the current study is to examine mechanical behavior of ABS 3D-printed parts under static and dynamic loads. To this end, ABS Carbon material is utilized to print the beam-like specimens with different mesostructures. Based on a series of bending and free-vibrations of the specimens, their performance and mechanical response are determined. In this study, we used the Digital Image Correlation (DIC) technique to measure local deformation on the specimens surface, and determine strain distribution and local displacements. On the numerical side, Finite Element (FE) simulation is employed to identify how stress distributions on different meso-configurations might affect bending rigidity and load carrying capacity of 3D-printed ABS cantilever beams with load at its tip under quasi static deformation. The FE analysis determines the best meso-shape(s) for 3D-printing structures under bending, and provides some insights in topology design of ABS 3D-printed structures with enhanced load carrying capacity under bending. The presented results can be used for optimization and further fabrication of FDM 3D-printed parts with a better mechanical behavior and structural performance. In the reminder of the paper we proceed as follows: the next section presents details of specimen design and preparation. In Section 3 the experimental tests are explained. Numerical simulations are outlined in Section 4. Discussion on the obtained results and verification of experiments are presented in Section 5. Finally, a conclusion has been furnished in Section 6.

2. Specimen preparation

In the present study, two groups of specimens are designed and fabricated: (i) dumbbell-shaped, and (ii) beam-like 3D-printed test coupons. For fabrication of all specimens, ABS Carbon material (Carbon fiber filled ABS: ABS-CF10) [32] is used, which combined the advantages of carbon fiber filament with favorable mechanical properties and ease of use of ABS material. The utilized ABS Carbon material is an engineering thermoplastic with exceptional strength and stiffness. The dumbbell-shaped specimens are designed according to type IV in ASTM D638 [33]. These test coupons are printed with thickness of 4 mm and 45°/–45° raster direction. The dumbbell-shaped specimens are fabricated and examined to obtain basic mechanical properties based on the tensile tests. Table 1 summarizes the printing parameters and the material parameters of the utilized ABS Carbon.

Since printing parameters have effects on the mechanical behavior of 3D-printed components, all printing parameters (e.g., infill density, layer thickness, and feed rate) were kept constant in fabrication of the test coupons. In this study, we printed and examined three dumbbell-shaped samples. Fig. 1 shows the schematic of dumbbell-shaped tensile test specimen.

Table 1

Properties of utilized ABS Carbon [32] and the printing parameters of dumbbell-shaped tensile test specimens.

Material parameters	Values	Printing parameters	Values
Specific gravity	1.097	Raster angle (°)	45/–45
Elongation at break (%)	2.7	Infill percentage (%)	100
Tensile yield strength (MPa)	21.2	Printing speed (mm/s)	100
Tensile elastic modulus (GPa)	3.342	Layer thickness (mm)	0.254
Compression modulus (GPa)	2.129	Bed temperature (°C)	100
Impact energy (notched) (J/m)	51.4	Nozzle temperature (°C)	250

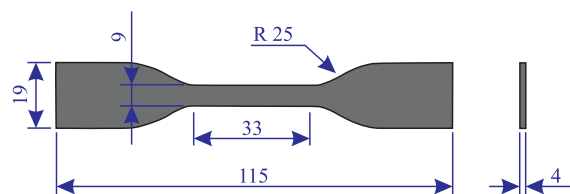


Fig. 1. Schematic of a dumbbell-shaped specimen (dimensions in mm).

The second group of the test coupons (beam-like specimens) are designed with four different mesostructures. For fabrication of the beam-like specimens, the Stratasys F190CR 3D printer is used, which is a user-friendly and cost-effective high strength composite printing equipment. This printer is equipped with hardened components to operate with composite materials. It is capable of printing both model and support material. The F190CR printer has a maximum build area of 305 × 254 × 305 mm with 2 material spool bays, 1 for model and 1 for support. The system weighs 227 kg and tolerance of ± 0.2 mm. The schematics of the beam-like specimens with four different mesostructures are illustrated in Fig. 2. It should be pointed out that the visual appearance of 3D-printed specimens parts were investigated to ensure the specimens were fabricated correctly. In the present study, three samples for each types of beam-like specimens were designed and fabricated. All specimens have a base dimension of 102.4 × 22 mm. The specimens are combined with a gripping area of dimensions 40 × 22 mm to be fixed on the instrument. The specimens were tested to ensure the repeatability and provide representative results. All test coupons were subjected to the experimental tests, which is explained in the following section.

3. Experimental tests

3.1. Tensile tests of 3D-printed dumbbell-shaped specimens

The tensile tests of dumbbell-shaped specimen were conducted in accordance with the ASTM D638 standard with the head displacement rate of 1 mm/min. The average results obtained from three repeated tests is used to provide information for evaluating the 3D-printed materials' performance.

3.2. Static and dynamic tests of 3D-printed beam-like specimens

A series of tests on the beam-like specimens is conducted using the Instron 50 kN load cell universal testing machine. A fixture was designed using a 100 mm × 50 mm aluminum block with two M5 tapered screws at the front to tighten the sample and two M10 holes to fix the fixture to a T-slot fixture. The fixture had an opening on the right side with a 22 mm height and 40 mm length for the gripping area of the sample to slide in. Once the fixture was ready, testing on the samples was done with a head displacement rate of 1 mm/min, as shown in Fig. 3.

In the experiment on the four beam-like specimens, each sample was mounted on the T-slot fixture. To carry out the optical measurements, a speckle pattern was prepared by black dots over a white background

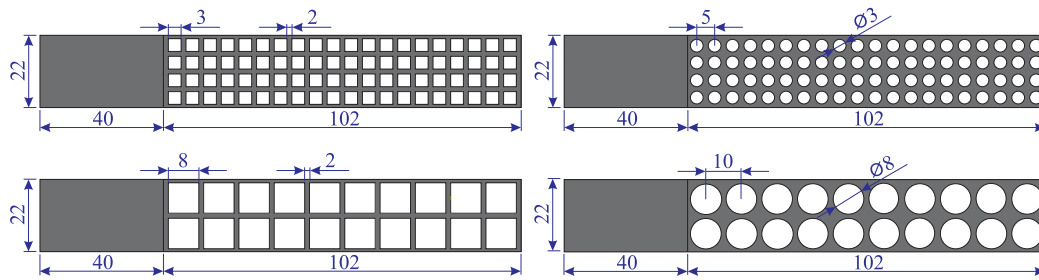


Fig. 2. Schematics of beam-like specimens with different mesostructures (dimensions in mm).

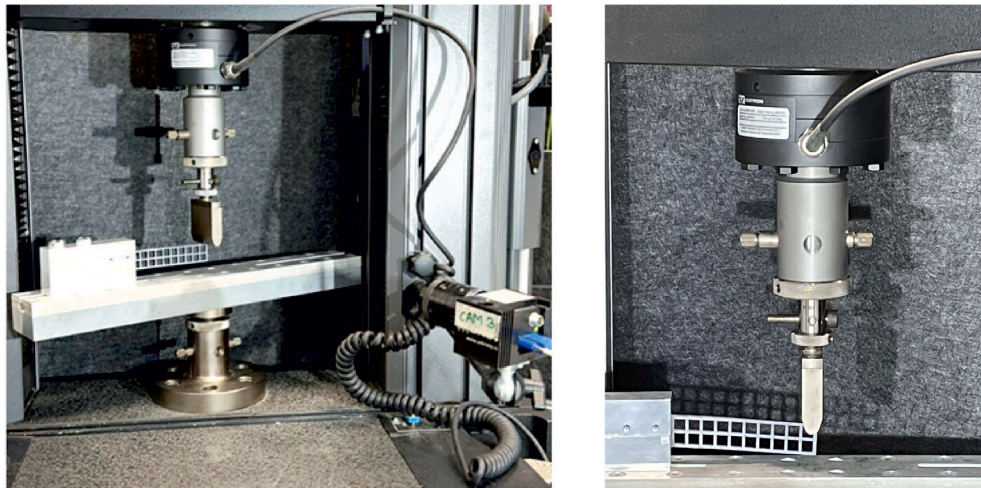


Fig. 3. Quasi-static test view of beam-like specimens mounted on the T-slot fixture; angled view (left) and front view (right).

spray painted on 3D-printed specimens. The samples were then introduced to a gradual load set to obtain specimen failure within 1 to 10 min. The deformation of the specimen was measured utilizing the DIC technique. In order to determine the material parameters, during the experiments, the photos of the specimens were taken at a 2-second interval and processed. A digital single-lens camera with a matrix resolution of 6000×4000 pixels was used to capture the images. The camera was equipped with a Sigma 17–50 mm f/2.8 AF EX DC OS HSM zoom lens with a focal length set at about 16 mm to cover the entire surface of the samples. The surface of the specimen was additionally illuminated with a white LED light source with a neutral hue of about 6000 K. The above process is repeated for 12 samples, three samples per specimen type. The universal testing machine recorded the force–displacement response. Moreover, optical documentation of the deformation for bending analysis was accompanied by a camera for DIC analysis as seen in Fig. 4.

The beam-like specimens were excited into free vibrations in order to perform a vibration test. The specimens were hit with a modal impact hammer, which produced short-duration excitation upon impact with the structure as shown in Fig. 5. A soft-force tip was used in the hammer in order to obtain a smaller bandwidth of frequencies, which therefore resulted in fewer double hits. An accelerometer was fixed at the free end of the specimen with wax in order to obtain the acceleration data via the ObservviewVR1000 software. The force data was obtained via the software from the hammer's force sensor. The data was captured using the roving hammer method, where the accelerometer stays in place and the hammer impacts the specimens at different points. Five points were chosen where the hammer was struck three times at each location, thus acquiring 15 sets of measurements in total for each specimen. A threshold force of 20 N and a frequency range of 0–1000 Hz were set. The data was directly transferred to the computer through the data acquisition system, where Frequency Response Function (FRF) graphs were obtained using the ObservviewVR1000 software.

4. Numerical simulations

To investigate how different topologies could impact the load-carrying performance of a 3D-printed ABS Carbon cantilever beam, Finite Element (FE) simulation is employed using the commercial FE package ABAQUS[®]. 3D geometrical models of cantilever beams with different meso-patterns (as depicted in Fig. 2) are built and precisely meshed using a 20-node quadratic brick (Hex) element C3D20R [34]. As quadratic elements are more accurate to capture stress and strain variations around the corners and curvatures of the model, and according to the shapes of the meso-beams chosen here, C3D20R is employed as a more accurate element compared to the similar types like C3D8R (8-node linear brick type element). It is also worth highlighting that the mesh size of elements is chosen precisely to fulfill the node-independency criteria of the FE models. This has been done through sensitivity analysis on the mesh size of the beams. The current global mesh size of all models is chosen as 0.8 mm. Fig. 6 shows the meshed model of a cantilever beam with four different meso-configurations: small square (B1), big square (B2), small circle (C1) and big circle (C2). The optimum global mesh size of all beams are considered as 0.8 mm to achieve the grid-independency criteria for all FE models. As demonstrated in Fig. 6, all nodes on the left side of the cantilever beams (40 mm from the left side) are considered to be fully fixed with all degrees of freedoms constrained. A uniform vertical displacement of U is applied on the top right corner of the beam. These boundary conditions match to the experimental conditions shown in Figs. 3. For mimicking the quasi-static status of the experiment, the static analysis of ABAQUS is used with non-linear mode activated. It is assumed that the vertical displacement at the right tip for all beams is of $U = 10$ mm and will be gradually applied to the structure.

The experimental force–displacement data of tensile tests of the standard dumbbell-shaped specimens (as shown in Fig. 1) are utilized, and the obtained strain–stress curve is illustrated in Fig. 7. This

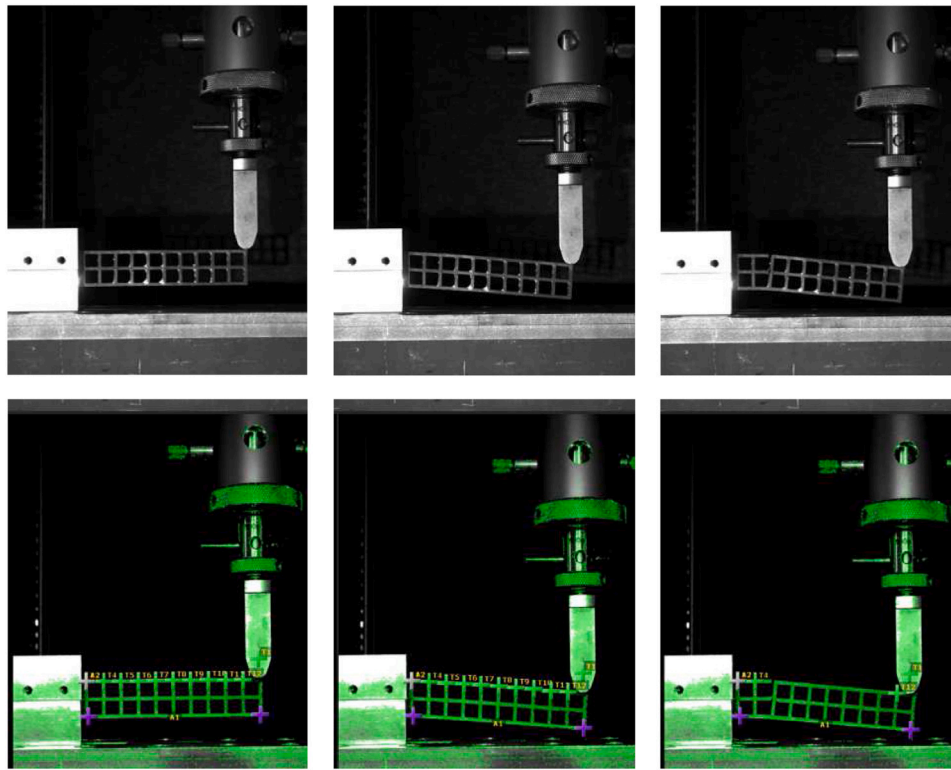


Fig. 4. DIC test analysis of beam-like specimens mounted on the T-slot fixture (from left to right) from the beginning till the maximum loading; grayscale image (top) and DIC software on (bottom).

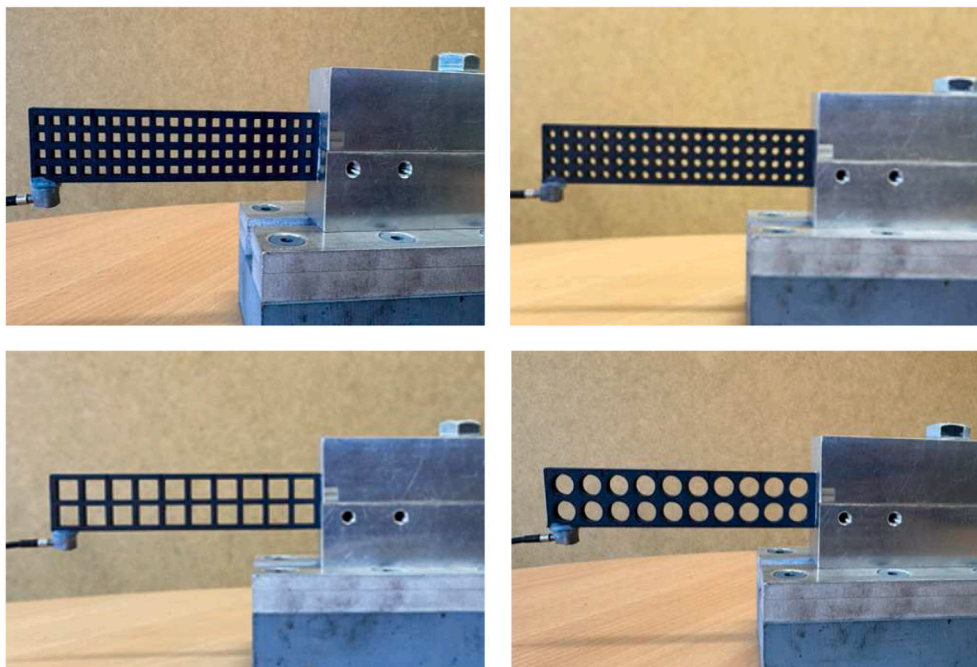


Fig. 5. Impact hammer test illustrations of 3D-printed mesostructured samples; small square (top left), small circle (top right), big square (bottom left), big circle (bottom right).

elasto-plastic stress–strain curve is then fed to the FE model of the beams demonstrating the material behaviors of 3D-printed ABS Carbon structures under the conditions given by Table 1.

The von-Mises stress distribution of a cantilever beam with four different meso-configurations (small square (B1), big square (B2), small circle (C1), and big circle (C2)) are shown in Figs. 8 at the tip deflection

of $U = 10$ mm. Although, the maximum von-Mises stress for all four different configuration is almost equal (around 38.5 MPa), occurring close to the top right of the beams; distributions of the stress is more uniform across the body of the small square (B1) and small circle (C1) beams compared to the other two. This clearly shows that the meso-pattern with smaller network of holes, facilitates the stress flow distributes evenly across the body of the beam and enhances its load-carrying

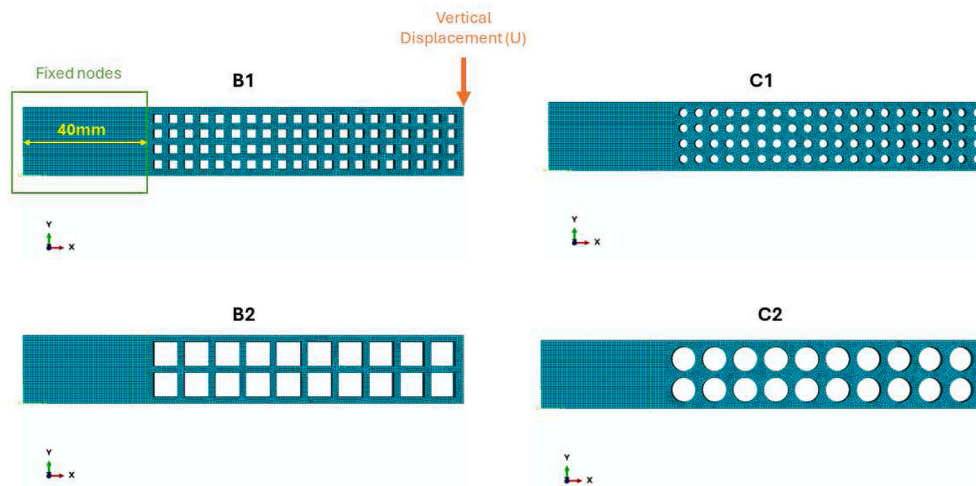


Fig. 6. 3D mesh model of the beams with four different microstructures: small square (B1), big square (B2), small circle (C1) and big circle (C2). All dimensions and geometrical details of these FE models are already given in Fig. 2.

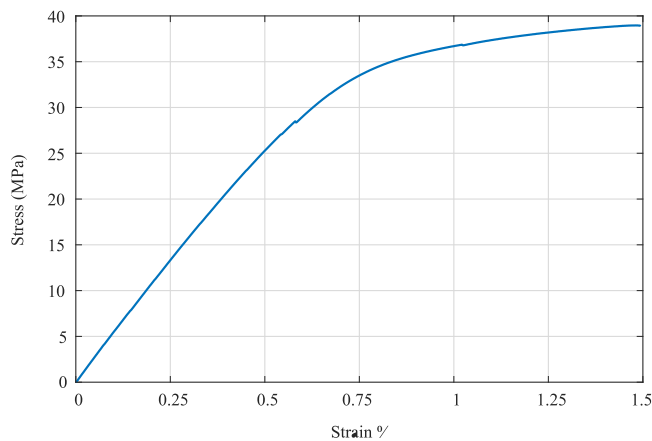


Fig. 7. Stress vs Strain curve of dumbbell-shaped tensile test ABS Carbon specimen as depicted in Fig. 1, according to the experimental force–displacement data.

capacities, accordingly. It is worth to highlight that the deflection of $U = 10 \text{ mm}$ is well beyond the elastic limit of the beams.

As ABS shows an elasto-plastic behavior (see Fig. 7), it is important to highlight how different regions of the beams might contribute to the load-carrying of the beams. Actively Yielding parameter (AC YIELD) is the element output defined in ABAQUS showing if an specific element undergoes plastic deformation or not. For the plastic flow zone, AC YIELD = 1, while for other areas AC YIELD = 0. In Fig. 9, AC YIELD contours for the four different meso-beams are shown at the deflection of $U = 10 \text{ mm}$. It is obvious that for the small circle (C1) and small square (B1), the focus of the plastic zone and plastic elements (red elements with AC YIELD = 1) are more uniform and close to the fixed point area. Hence, in this area, more elements are carrying higher stress (beyond their elastic limit), and more elements contribute to the load-carrying of the beams, consequently.

To reveal this fact more, the reaction force of the four cantilever meso-beams are plotted against the vertical displacement of the tip U . As it is shown in Fig. 10, the best load-carrying performance (with the highest level of reaction force), goes for the beam with small circle meso-structure (C1), where the maximum carrying load is obtained as 0.1132 kN. The beam with small square (B1) meso-structure is the next beam that shows a good load-carrying capacity with a maximum load of 0.0981 kN. The other two meso-beams with the big square (B2) and big circle (C2) carry the lowest maximum load of 0.07 kN and

Table 2
Maximum resultant force of the meso-beams obtained by the FE models and the experiments.

Meso-beam	F_{max} (kN)	
	FE	Experiment
Small square	0.0981	0.0915
Big square	0.0613	0.0653
Small circle	0.1132	0.0957
Big circle	0.07	0.086

Table 3
The average force and displacement data of the dumbbell-shaped specimens.

Max. Force (N)	Displacement at Max. Force (mm)	Max. Displacement (mm)
737.1	1.503	1.53

0.0613 kN, correspondingly. These important data are also validated with the experimental data and the same pattern is observed. Table 2 compares the FE and experimental result of the maximum reaction force for the four types of meso-beams.

5. Results and discussion

- Static test

The force and displacement data from the initial tensile tests that were conducted on the dumbbell-shaped specimens were obtained through the Instron software. Three dumbbell-shaped samples were tested in total, and the average of the three data points is used to plot the force–displacement graph in Fig. 11.

The data mentioned in Table 3 is used for conducting the FEA analysis on the beams. The average data of the samples of the beam is calculated, and force–displacement graphs are plotted in Fig. 11 and shown in Table 4 for the same. Using the force and weight data of the specimens, the force-to-weight ratio is calculated as inserted in Table 5.

From the results in Fig. 11, it is seen that the big square has the highest displacement among all the specimens, but at the same time has the least force-to-weight ratio of all. Whereas the small square has the least displacement but the highest force-to-weight ratio among all, indicating it is the stiffest one. The big circle has an optimum displacement and force-to-weight ratio value, comparatively. The small circle would be the least viable choice, as the force-to-weight ratio is comparatively poor when considering its weight. The data collected are for different geometries, but all the beams have the same volume as

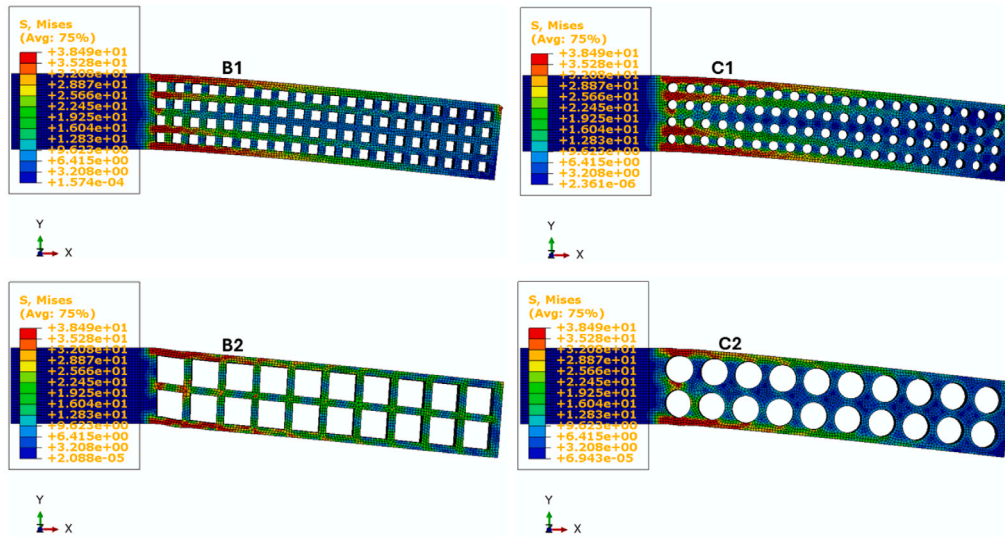


Fig. 8. von Mises stress distributions on FE models of meso-beams at the tip deflection of $U = 10$ mm with small square (B1), big square (B2), small circle (C1) and big circle (C2) configurations.

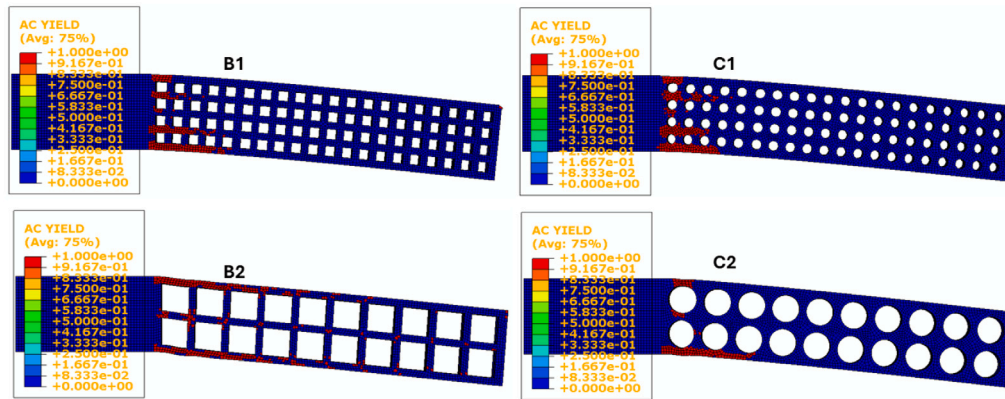


Fig. 9. Actively yield elements (AC Yield) of FE models of the meso-beam at the tip deflection of $U = 10$ mm with small square (B1), big square (B2), small circle (C1) and big circle (C2) configurations.

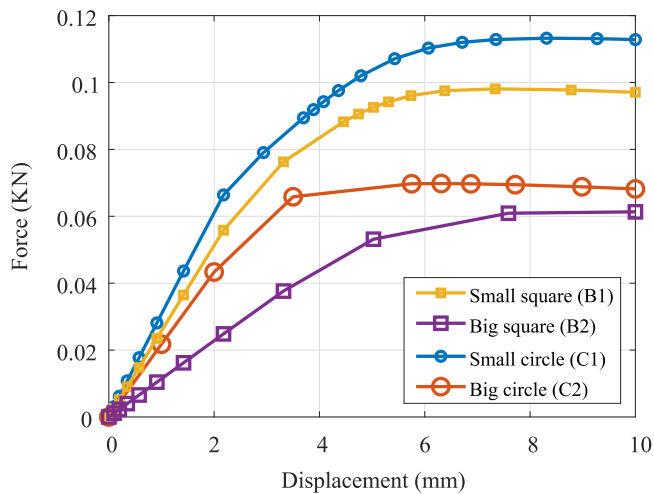


Fig. 10. Finite element resultant force-displacement curves of the meso-beams with different configurations.

Table 4

The average force and displacement data of the 3D-printed beam-like specimens.

Specimen	Max. Force (N)	Displacement at Max. Force (mm)
Small square	91.40	7.36
Big square	65.31	8.36
Small circle	95.73	7.14
Big circle	86.20	7.55

Table 5

The force-to-weight ratio of the specimens with various mesostructure.

Specimen	Force-to-Weight Ratio (N/kg)
Small square	8.9345
Big square	8.3133
Small circle	8.7946
Big circle	9.5554

they are all printed using the same material. The strength-to-weight ratio values are directly proportional to the infill density; the higher the infill density, the higher the strength-to-weight ratio values. But the drawback of using higher infill density implies that both raw material consumption and build time are high. Standard industrial

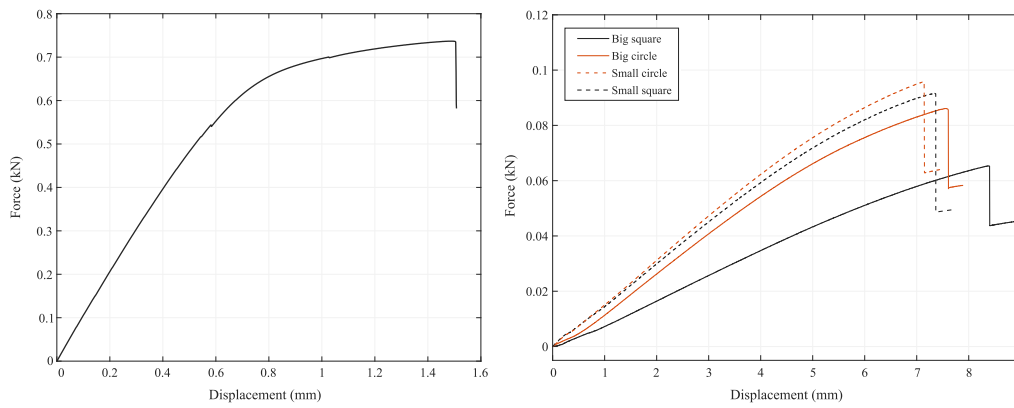


Fig. 11. Force–displacement response of examined dumbbell-shaped (left) and cantilever beams (right).

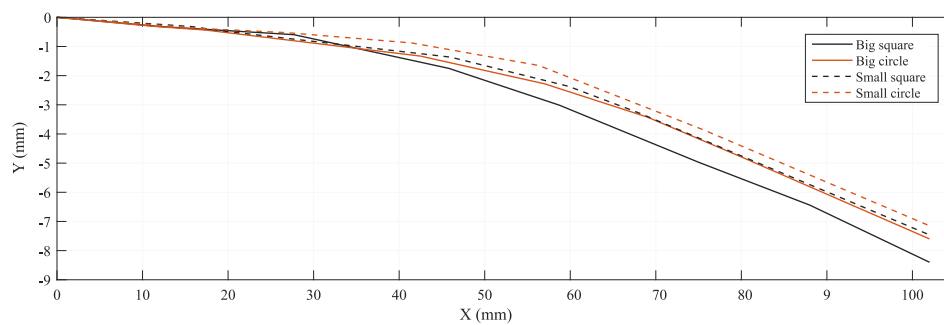


Fig. 12. Deflection results of the cantilever tips.

Table 6

The frequency results of the specimens with various mesostructures.

Small square	Big square	Small circle	Big circle
196.7 ± 2.5	202.8 ± 1.8	97.1 ± 2.3	228.5 ± 5.2

practice works on the principle of saving built time and material and reducing running costs without reducing the mechanical properties of FDM 3D-printed parts.

The data obtained from the optical measurements through DIC is shown in Fig. 12. The DIC technique indicated the experimental deflection lines. This the deflection line was measured on the top edge of the beam-like specimens by placing various point probes on the beam. The data is acquired right before the specimen breaks.

- Dynamic test

A graph of a representative set of measurements from the dynamic tests is illustrated in Fig. 13. After averaging five measurements, the FRF determined the dominant frequency. The FRF in ObserviewVR1000 is used to plot the frequency results of the beams in response to the hammer strikes, while the time domain results are demonstrated too. From the frequency results, in Table 6, it is evident that the beam that vibrated with the lowest frequencies is the small circle, whereas the beam that vibrated with the highest frequencies is the big circle, indicating that its mesostructure is the stiffest one (see Fig. 14).

The presented outcome of this study can be used to optimize the design and 3D-printed structural elements. Since the obtained results are validated by comparison of experimental tests and numerical simulation, the developed numerical models can be employed for further

numerical models and future computational modeling of 3D-printed parts.

6. Conclusion

In this contribution, mechanical behaviors of 3D-printed structural elements with different meso-patterns are investigated. The beam-like specimens with four different mesostructures are printed using ABS Carbon material. ABS carbon filament is chosen as one of the most popular materials being used in commercial 3D printers nowadays, and the popular FDM printing technique is employed to manufacture the beam-like elements. Four different meso-patterns (with small circles, big circles, small squares and big squares pattern) are chosen. The main objective of this research is to identify how different meso-patterns could have impact on the load carrying and dynamic characteristics of 3D-printed beam-like elements. Mechanical properties of printed ABS Carbon structures are experimentally extracted using a series of 3D-printed standard dumbbell-shaped coupons subjected to the standard universal tensile test. To measure static load carrying capacity of the meso-beams, standard cantilever bending test is conducted and modal test is employed to extract their natural frequencies. It is noteworthy that the deformations of the specimens are measured and reported based on the DIC technique.

In addition, FE simulation is performed to expand detailed knowledge on the impact of different topologies on the load-carrying performance of the examined 3D-printed ABS meso-structures. The results indicate that the beam-like specimen with small circle meso-structure indicates the best load-carrying performance (maximum force: 95.73 N). On the other hand, two beam-like specimens with big square and big circle mesostructure carry the lowest maximum load (65.31 and

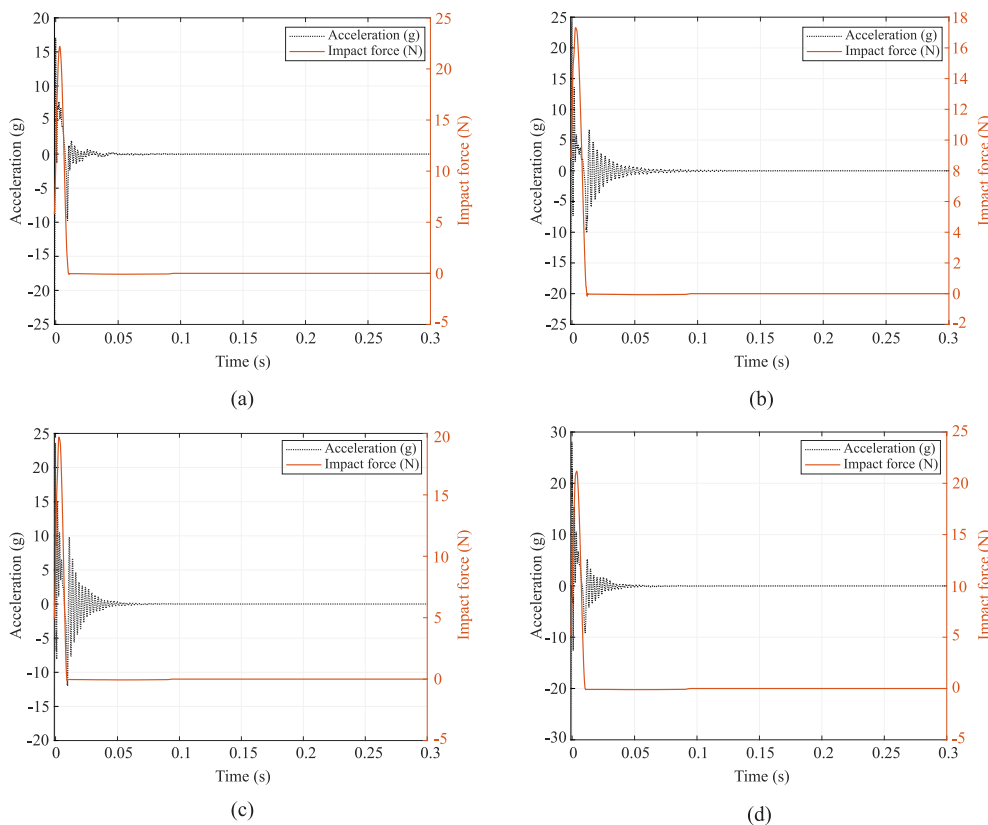


Fig. 13. Time response vibration results of the cantilever tips: (a) small square, (b) big square, (c) small circle, and (d) big circle.

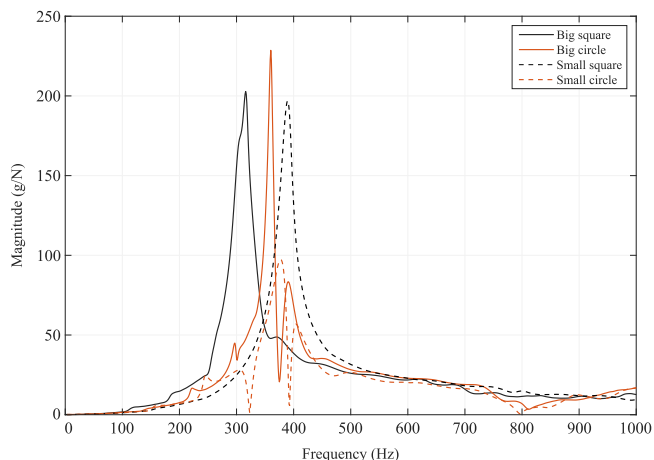


Fig. 14. Frequency vibration results of the cantilever tips.

86.20 N, respectively). Considering the range of values obtained from both tests (bending and modal tests) and computational FE models, technical insights are provided to the structural and material designers in selecting the best topology, desired stiffness and enhanced load-carrying capacities of ABS Carbon 3D-printed structures on the specific application needs.

CRedit authorship contribution statement

Mohammad Reza Khosravani: Writing – review & editing, Project administration, Methodology, Conceptualization, Supervision. **Payam**

Soltani: Writing – review & editing, Software, Formal analysis. **Bernard Rolfe:** Resources, Writing – original draft. **Tamara Reinicke:** Writing – review & editing, Funding acquisition. **Ali Zolfagharian:** Writing – original draft, Resources, Investigation, Validation.

Declaration of competing interest

The authors declare that they have no known competing financial interests or personal relationships that could have appeared to influence the work reported in this paper.

Data availability

Data will be made available on request.

References

- [1] A.A. Mohammed, M.S. Algahtani, M.Z. Ahmad, S. Kotta, 3D printing in medicine: Technology overview and drug delivery applications, *Ann. 3D Print. Med.* 4 (2021) 100037.
- [2] S. Agarwala, G.L. Goh, Y. Yap, G. Goh, H. Yu, W. Yeong, T. Tran, Development of bendable strain sensor with embedded microchannels using 3D printing, *Sensors Actuators A* 263 (2017) 593–599.
- [3] S. Mantihal, R. Kobun, B.B. Lee, 3D food printing of as the new way of preparing food: A review, *Int. J. Gastron. Food Sci.* 22 (2020) 100260.
- [4] M.R. Khosravani, A. Haghighi, Large-scale automated additive construction: Overview, robotic solutions, sustainability, and future prospect, *Sustainability* 14 (2022) 9782.
- [5] V. Mohanavel, K.A. Ali, K. Ranganathan, J. Jeffrey, M.M. Ravikumar, The roles and applications of additive manufacturing in the aerospace and automobile sector, *Mater. Today. Proc.* 47 (2021).
- [6] G. Stano, G. Percoco, Additive manufacturing aimed to soft robots fabrication: A review, *Extreme Mech. Lett.* 42 (2021) 101079.
- [7] K.V.P. Reddy, I.M. Mirzana, A.K. Reddy, Application of additive manufacturing technology to an aerospace component for better trade-offs, *Mater. Today Proc.* 5 (2018) 3895–3902.

- [8] ISO/ASTM-52900, Additive manufacturing - General principles - Fundamentals and vocabulary, ASTM International, 2021.
- [9] M. Kariz, M. Sernek, M. Obucina, M.K. Kuzman, Effect of wood content in FDM filament on properties of 3D printed parts, *Mater. Today Commun.* 14 (2018) 135–140.
- [10] R. Chen, W. He, H. Xie, S. Liu, Monitoring the strain and stress in FDM printed lamellae by using fiber Bragg grating sensors, *Polym. Test.* 93 (2021) 106944.
- [11] G. Atakok, M. Kam, H.B. Koc, Tensile, three-point bending and impact strength of 3D printed parts using PLA and recycled PLA filaments: A statistical investigation, *J. Mater. Res. Technol.* 18 (2022) 1542–1554.
- [12] M.R. Khosravani, S. Rezaei, S. Faroughi, T. Reinicke, Experimental and numerical investigations of the fracture in 3D-printed open-hole plates, *Theor. Appl. Fract. Mech.* 121 (2022) 103543.
- [13] Z. Yan, Y. Liu, J. Yan, W. Wu, F. Bai, F. Huang, Blast performance of 3D-printed auxetic honeycomb sandwich beams, *Thin Wall Struct.* 193 (2023) 111257.
- [14] M. Bragaglia, F. Cecchini, L. Paleari, M. Ferrara, M. Rinaldi, F. Nanni, Modeling the fracture behavior of 3D-printed PLA as a laminate composite: Influence of printing parameters on failure and mechanical properties, *Compos. Struct.* 322 (2023) 117379.
- [15] M.N. Ahmad, M.R. Ishak, M.M. Taha, F. Mustapha, Z. Leman, I. Irianto, Mechanical, thermal and physical characteristics of oil palm (*Elaeis Guineensis*) fiber reinforced thermoplastic composites for FDM - Type 3D printer, *Polym. Test.* 120 (2023) 107972.
- [16] S. Shahbaz, M.R. Ayatollahi, M. Petru, A.R. Torabi, U-notch fracture in additively manufactured ABS specimens under symmetric three-point bending, *Theor. Appl. Fract. Mech.* 119 (2022) 103318.
- [17] A.G. Stamopoulos, S.I. Scipioni, F. Lambiasi, Experimental characterization of the interlayer fracture toughness of FDM components, *Compos. Struct.* 320 (2023) 117213.
- [18] M.R. Khosravani, P. Soltani, T. Reinicke, Effects of steps on the load bearing capacity of 3D-printed single lap joints, *J. Mater. Res. Technol.* 23 (2023) 1834–1847.
- [19] J. Agnelli, C. Pagano, I. Fassi, L. Treccani, F. Bignotti, F. Baldi, Mechanical behaviour of ductile polymer cellular model structures manufactured by FDM, *Mech. Mater.* 190 (2024) 104882.
- [20] M.R. Khosravani, F. Berto, M.R. Ayatollahi, T. Reinicke, Characterization of 3D-printed PLA parts with different raster orientations and printing speeds, *Sci. Rep.* 12 (2022) 1016.
- [21] A.C. Bruijn, G. Gomez-Gras, L. Fernandez-Rouano, L. Farras-Tasias, M.A. Perez, Optimization of a combined thermal annealing and isostatic pressing process for mechanical and surface enhancement of ultem FDM parts using doehlert experimental designs, *J. Manuf. Processes* 85 (2023) 1096–1115.
- [22] M.R. Karamooz Ravari, M. Kadkhodaei, M. Badrossamay, R. Rezaei, Numerical investigation on mechanical properties of cellular lattice structures fabricated by fused deposition modeling, *Int. J. Mech. Sci.* 88 (2014) 154–161.
- [23] Y.T. Kao, Y. Zhang, J. Wang, B.L. Tai, Bending behaviors of 3D-printed Bi-material structure: Experimental study and finite element analysis, *Addit. Manuf.* 16 (2017) 197–205.
- [24] M. Somireddy, A. Czekanski, C.V. Singh, Development of constitutive material model of 3D printed structure via FDM, *Mater. Today Commun.* 15 (2018) 143–152.
- [25] M.R. Khosravani, P. Soltani, K. Weinberg, T. Reinicke, Structural integrity of adhesively bonded 3D-printed joints, *Polym. Test.* 100 (2021) 107262.
- [26] J.F. Rodriguez, J.P. Thomas, J.E. Renaud, Mechanical behavior of acrylonitrile butadiene styrene fused deposition materials modeling, *Rapid Protot. J.* 9 (2003) 219–230.
- [27] M. Kucwicz, P. Baranowski, M. Stankiewicz, M. Konarzewski, P. Platek, J. Malachowski, Modelling and testing of 3D printed cellular structures under quasi-static and dynamic conditions, *Thin Wall Struct.* 145 (2019) 106385.
- [28] Y. Zhang, J.P. Choi, S.K. Moon, Effect of geometry on the mechanical response of additively manufactured polymer, *Polym. Test.* 100 (2021) 107245.
- [29] M.R. Khosravani, P. Soltani, T. Reinicke, Fracture and structural performance of adhesively bonded 3D-printed PETG single lap joints under different printing parameters, *Theor. Appl. Fract. Mech.* 116 (2021) 103087.
- [30] A. Corvi, L. Collini, Combined RVE-cohesive elements approach to the multi-scale modelling of FDM 3D-printed components, *Theor. Appl. Fract. Mech.* 128 (2023) 104140.
- [31] A. Garg, A. Bhattacharya, An insight to the failure of FDM parts under tensile loading: Finite element analysis and experimental study, *Int. J. Mech. Sci.* 120 (2017) 225–236.
- [32] Introduction to digital image correlation and strain computation, 2024, <https://www.stratasy.com/en/materials/materials-catalog/fdm-materials/abs-cf10>, (Accessed 18 January 2024).
- [33] ASTM D638-14 Standard Test Method for Tensile Properties of Plastics, Standard, American Society for Testing Materials, West Conshohocken, USA, 2014.
- [34] G. Abaqus, Abaqus 6.11, Dassault Systemes Simulia Corporation, Providence, RI, USA 3, 2011.